

Distinct spin and orbital dynamics in Sr_2RuO_4

Received: 24 March 2023

Accepted: 20 October 2023

Published online: 03 November 2023

 Check for updates

H. Suzuki ^{1,2,3,15} ✉, L. Wang ^{1,15}, J. Bertinshaw¹, H. U. R. Strand ^{4,5}, S. Käser^{1,6}, M. Krautloher ¹, Z. Yang¹, N. Wentzell ⁷, O. Parcollet^{7,8}, F. Jerzembeck ⁹, N. Kikugawa ¹⁰, A. P. Mackenzie ⁹, A. Georges^{7,11,12,13}, P. Hansmann ^{1,6,9}, H. Gretarsson^{1,14} ✉ & B. Keimer ¹ ✉

The unconventional superconductor Sr_2RuO_4 has long served as a benchmark for theories of correlated-electron materials. The determination of the superconducting pairing mechanism requires detailed experimental information on collective bosonic excitations as potential mediators of Cooper pairing. We have used Ru L_3 -edge resonant inelastic x-ray scattering to obtain comprehensive maps of the electronic excitations of Sr_2RuO_4 over the entire Brillouin zone. We observe multiple branches of dispersive spin and orbital excitations associated with distinctly different energy scales. The spin and orbital dynamical response functions calculated within the dynamical mean-field theory are in excellent agreement with the experimental data. Our results highlight the Hund metal nature of Sr_2RuO_4 and provide key information for the understanding of its unconventional superconductivity.

Conduction electrons in quantum materials form itinerant quasi-particles that propagate coherently over mesoscopic length scales, while being renormalized by local interactions akin to those in atomic physics. This dichotomy spawns a large variety of collective quantum phenomena and remains one of the major challenges of modern condensed matter physics, as epitomized by the Hubbard model describing electrons on a lattice with a single orbital per site, which has defied a complete solution until today—60 years after it was first introduced. Coulomb repulsion of opposite-spin electrons residing on the same site drives the electron system toward a Mott insulating state and induces antiferromagnetic spin correlations, which have been invoked as a mediator of Cooper pairing in unconventional

superconductors such as cuprates¹ and nickelates². Whereas bona-fide realizations of the Hubbard model are rare, studies on transition metal oxides³ and iron-based superconductors⁴ have led to the realization that atomic Hund's rule interactions among conduction electrons with multiple active d -orbitals are a source of strong electron correlations. In principle, treating spin and orbital correlations on an equal footing further increases the challenge in the theoretical description of the interacting electron system. However, recent dynamical mean-field theory (DMFT) studies of the broad family of “Hund metals”⁵ have suggested that the Hund's rule interactions drive a large-scale differentiation of spin and orbital screening energies^{6,7}. Indirect manifestations of this “spin-orbital separation” include the formation of local

¹Max-Planck-Institut für Festkörperforschung, Heisenbergstraße 1, D-70569 Stuttgart, Germany. ²Frontier Research Institute for Interdisciplinary Sciences, Tohoku University, Sendai 980-8578, Japan. ³Institute of Multidisciplinary Research for Advanced Materials (IMRAM), Tohoku University, Sendai 980-8578, Japan. ⁴School of Science and Technology, Örebro University, Fakultetsgatan 1, SE-701 82 Örebro, Sweden. ⁵Institute for Molecules and Materials, Radboud University, 6525 AJ Nijmegen, the Netherlands. ⁶Department of Physics, Friedrich-Alexander-University (FAU) of Erlangen-Nürnberg, 91058 Erlangen, Germany. ⁷Center for Computational Quantum Physics, Flatiron Institute, Simons Foundation, 162 5th Avenue, New York 10010, USA. ⁸Université Paris-Saclay, CNRS, CEA, Institut de physique théorique, 91191 Gif-sur-Yvette, France. ⁹Max Planck Institute for Chemical Physics of Solids, Nöthnitzer Straße 40, 01187 Dresden, Germany. ¹⁰National Institute for Materials Science, Tsukuba, Ibaraki 305-0003, Japan. ¹¹Collège de France, 11 place Marcelin Berthelot, 75005 Paris, France. ¹²Centre de Physique Théorique (CPHT), CNRS, Ecole Polytechnique, IP Paris, 91128 Palaiseau, France. ¹³Department of Quantum Matter Physics, University of Geneva, 24 Quai Ernest-Ansermet, 1211 Geneva 4, Switzerland. ¹⁴Deutsches Elektronen-Synchrotron DESY, Notkestraße 85, D-22607 Hamburg, Germany. ¹⁵These authors contributed equally: H. Suzuki, L. Wang. ✉e-mail: hakuto.suzuki@tohoku.ac.jp; hlynur.gretarsson@desy.de; b.keimer@fkf.mpg.de

magnetic moments and the anomalously low onset temperature of the coherent Fermi-liquid state in iron-based superconductors.

Here we report a direct spectroscopic fingerprint of spin-orbital separation in the archetypical Hund metal Sr_2RuO_4 ⁸, which has been the subject of many years of study in view of the textbook Fermi-liquid transport properties⁹ and unconventional superconducting state¹⁰ that develop upon cooling below the coherence temperature $T_{\text{coh}} \sim 25$ K and critical temperature $T_c = 1.5$ K, respectively. Recent precision experiments in the superconducting state^{11–13} have cast doubt on the previously advocated spin-triplet pairing scenario^{14,15}, thus revitalizing the order parameter debate¹⁶ and the search for an in-depth understanding of the Fermi-liquid normal state and collective bosonic fluctuations relevant to superconductivity. The lattice structure of Sr_2RuO_4 is built up of RuO_6 octahedra in a square-planar arrangement, and its Fermi surface comprises three bands originating from the d -orbital manifold of Ru^{4+} ions in the octahedral crystal field. Owing to the availability of exceptionally clean single crystals, the electronic quasiparticle properties in these bands are very well known and clearly indicate strong electronic correlations. The temperature dependence of the Seebeck coefficient^{17,18} suggests a separation between energy scales associated with the onset of coherence of spin and orbital degrees of freedom, consistent with the notion that these correlations are governed by Hund's rules^{19,20}. Inelastic neutron scattering (INS) studies of Sr_2RuO_4 ^{21–24} have revealed low-energy incommensurate spin fluctuations (ISFs) at the in-plane wavevectors $\mathbf{q}_{\text{ISF}} = (\pm 0.3, \pm 0.3)$ and along a square-shaped ridge connecting them (Fig. 1a, inset). However, the INS spectra are limited to energies below ~ 50 meV and do not yield separate information on orbital excitations.

We have used Ru L_3 -edge (2838 eV) resonant inelastic x-ray scattering (RIXS) to obtain spectroscopic maps of spin and orbital fluctuations over a wide range of energy and momenta. Whereas the spin excitations are almost completely confined to energies below ~ 200 meV, significant orbital fluctuations only appear at higher energies and extend up to ~ 1 eV, thus directly confirming the theoretically predicted spin-orbital separation. The RIXS spectra disagree starkly with predictions based on the standard random phase approximation (RPA), which do not capture the distinct energy scales of spin and orbital correlations, but are in excellent agreement with calculations in the framework of DMFT, which takes into account vertex corrections. Our results thus demonstrate the key role of Hund's-rule interactions in inducing electron correlations in multiband metals, and highlight the capability of current many-body theory to accurately compute two-particle correlation functions. They also shed light on the nature

of potential pairing bosons for unconventional superconductivity in Sr_2RuO_4 .

Results and discussion

Figure 1a shows the crystal structure of Sr_2RuO_4 and the scattering geometry for the RIXS experiment. The incident x-ray photons were π -polarized, and the scattered photons with both σ and π polarizations were collected at the scattering angle of 90 degrees. In this geometry, the polarizations of the incident and outgoing photons are always perpendicular, selectively enhancing magnetic responses from the spin and orbital excitations while suppressing the charge response. Given the layered crystal structure of Sr_2RuO_4 , we express the momentum transfer using the in-plane component \mathbf{q} , which is scanned by changing the sample angle θ . We studied two paths in the reciprocal space, $\mathbf{q} = (H, 0)$ and (H, H) , by fixing the azimuthal angle ϕ at 0° and -45° , respectively. These paths cross the ridge and the peak of the low-energy ISFs (inset). The measurements were performed at $T = 25$ K, in the FL regime of the normal state.

In Fig. 1b, we show the Ru L_3 RIXS spectra along the two directions. Multiple peak structures are readily identified. The main feature A is composed of multiple peaks which extend up to ~ 1 eV. These peaks are assigned to spin and orbital excitations within the t_{2g} orbitals. In addition, a weakly-dispersive feature B is identified at ~ 3 eV (blue circles). As this energy corresponds to the splitting of the transitions to the unoccupied $4d$ t_{2g} and e_g orbitals in the Ru L_3 x-ray absorption spectrum (Supplementary Fig. 1a), the feature B is readily assigned to the crystal field transitions to the $t_{2g}^3 e_g^1$ electron configurations. We note here that its intensity is maximal close to the $\mathbf{q} = (0, 0)$ point along the two directions.

To visualize the characteristics of the RIXS spectra, we show in Fig. 1c a colormap of the RIXS intensity. The main feature A is composed of multiple dispersions. Its low-energy tail exhibits downward dispersion toward its local minima at $\mathbf{q} = (-0.3, 0)$ and $(-0.7, 0)$ along the $(H, 0)$ direction and at $\mathbf{q}_{\text{ISF}} = (-0.3, -0.3)$ along the (H, H) direction (white triangles). These \mathbf{q} vectors are in excellent agreement with those of the ridges and ISFs identified in the previous INS studies^{23,24}. However, the information from the INS data is limited to the low-energy region below ~ 0.1 eV, whereas the full access to a large energy window in the present RIXS experiment provides comprehensive information on the ISFs. The relative intensity of spin excitations and the location of the ISF are determined by the nesting conditions between the multiple Fermi surface sheets of Sr_2RuO_4 . It is well established that the nesting between the α and β sheets with \mathbf{q}_{ISF} , as

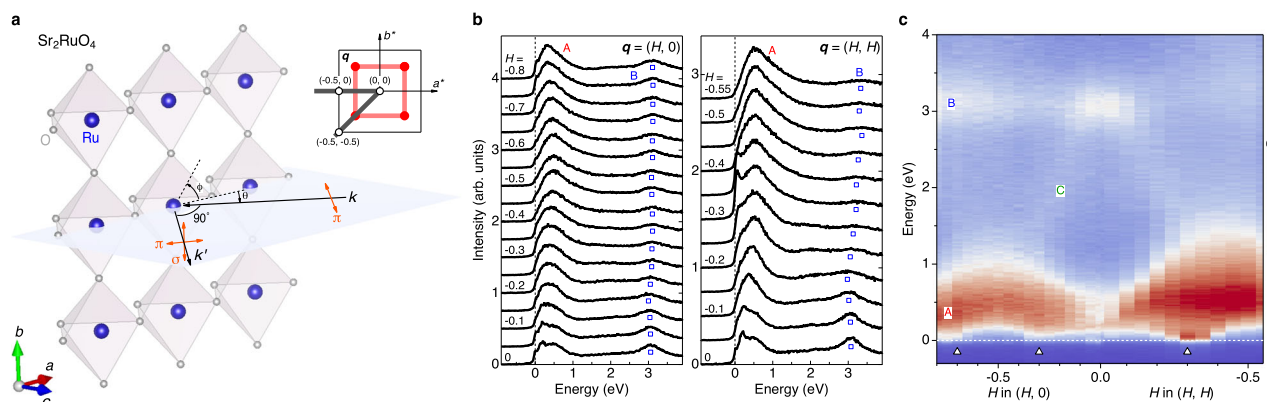


Fig. 1 | Ru L_3 RIXS of Sr_2RuO_4 . **a** Crystal structure of Sr_2RuO_4 and scattering geometry for the resonant inelastic x-ray scattering (RIXS) experiment. Incident x-ray photons with momentum \mathbf{k} are linearly π -polarized and the polarization of the scattered photons with momentum \mathbf{k}' is not analyzed. The scattering angle is fixed at 90° and the in-plane momentum transfer \mathbf{q} is scanned by rotating the sample angle θ . The azimuthal angle ϕ is used to change the measurement paths in the

reciprocal space (gray lines, inset). Red circles and lines in the inset are the schematics of the low-energy incommensurate spin fluctuations (ISFs). **b** Ru L_3 RIXS spectra along the $\mathbf{q} = (H, 0)$ and (H, H) directions. Blue squares indicate the peak positions of crystal field transitions. **c** Colormap of RIXS intensity. The positions of ISFs are indicated by open triangles.

demonstrated by angle-resolved photoemission measurements²⁵, drives the incommensurate spin fluctuations with \mathbf{q}_{ISF} ²⁶. In contrast, the nesting is only partial along the $(H, 0)$ direction, resulting in the reduced intensity of the spin fluctuations along this direction.

The colormap also reveals an additional broad dispersive feature C at high energy (≥ 1 eV). It emanates from the top of the feature A at $\mathbf{q} = (-0.5, 0)$ and $(-0.5, -0.5)$ and merges with the feature B at the $(0, 0)$ point, generating the intensity maximum. At the high-symmetry $(0, 0)$ point, the dd excitations to the $d_{x^2-y^2}$ and $d_{3z^2-r^2}$ orbitals remain localized and are almost degenerate in energy under the small tetragonal distortion of the RuO_6 octahedra. At finite in-plane \mathbf{q} 's, the excitations to the planar $d_{x^2-y^2}$ orbitals show energy dispersion due to large overlap integrals with the planar O $2p$ orbitals, while those to the out-of-plane $d_{3z^2-r^2}$ orbitals have little in-plane dispersion due to the small overlap integrals. The nondispersive feature B and dispersive feature C are thus primarily ascribed to the transitions to the $d_{3z^2-r^2}$ and $d_{x^2-y^2}$ orbitals, respectively. The dispersion of the orbital fluctuations originates from the large bandwidth of Sr_2RuO_4 with a tetragonal crystal structure. In contrast, the nondispersive orbital excitations observed in orthorhombic Ca_2RuO_4 ²⁷ and $\text{Ca}_3\text{Ru}_2\text{O}_7$ ²⁸ indicate that the local dd excitations cannot freely move to the neighboring sites, as the rotation of the RuO_6 octahedra significantly reduces the hopping integrals.

Having identified multiple branches of spin-orbital excitations in Sr_2RuO_4 , we now scrutinize the low-energy excitations within the t_{2g} orbitals (feature A). Figure 2a shows an expanded plot of the RIXS spectra below 0.8 eV. The broad global peak maxima (red circles) disperse from 0.2 eV at the zone center $\mathbf{q} = (0, 0)$, where they are most sharply peaked, to the maximal energy at the zone boundary, $\mathbf{q} = (0, -0.5)$ and $(-0.5, -0.5)$. We ascribe this dispersion to orbital

fluctuations as we will see below. The energy scale of orbital fluctuations near the zone center agrees with that of the O K -edge RIXS data²⁹. Along the (H, H) direction, the low-energy region contains prominent peaks due to the ISFs around $\mathbf{q}_{\text{ISF}} = (-0.3, -0.3)$ and subsequent shoulder structures connected to the $(0, 0)$ point, as indicated with black circles (Supplementary Note 2). The quasielastic intensity at the $(0, 0)$ point is significantly weaker than at \mathbf{q}_{ISF} , consistent with polarized INS data²². On the other hand, the spin fluctuation intensity is weaker along the $(H, 0)$ direction, except for the small increase of the quasi-elastic intensity of the ridge scattering around $(-0.3, 0)$ and $(-0.7, 0)$ ^{23,24}. In addition, the spectra close to the $(0, 0)$ point contain a broad high-energy tail peaked around -0.5 eV (Supplementary Note 5).

Figure 2b summarizes the \mathbf{q} dispersions of the observed RIXS features. Here, the dispersion of the orbital fluctuations is defined as the global peak maxima of the RIXS spectra, and that of the spin fluctuations as the local maxima of spectral curvature deduced from the second derivative analysis (Supplementary Fig. 2). Along the $(H, 0)$ direction, the orbital fluctuations disperse from -0.2 eV at the $(0, 0)$ point and reach the maximum of -0.5 eV at the $(-0.5, 0)$ point. Along the (H, H) direction, the dispersion is initially steeper and becomes almost flat in the region $H \leq -0.25$ at a higher energy -0.55 eV. The spin excitations have a local minimum of 0.06 eV at $\mathbf{q}_{\text{ISF}} = (-0.3, -0.3)$ and approach zero energy close to the $(0, 0)$ point. Note here that the spin and orbital fluctuations have distinct energy scales in the entire \mathbf{q} space without a clear signature of mutual crossing. This observation is of crucial importance in testing the validity of different theoretical approaches.

To facilitate a direct connection to the INS results, we show in Fig. 2c an expanded colormap of the RIXS intensity around \mathbf{q}_{ISF} and corresponding energy distribution curves with a step size of 0.02 eV.

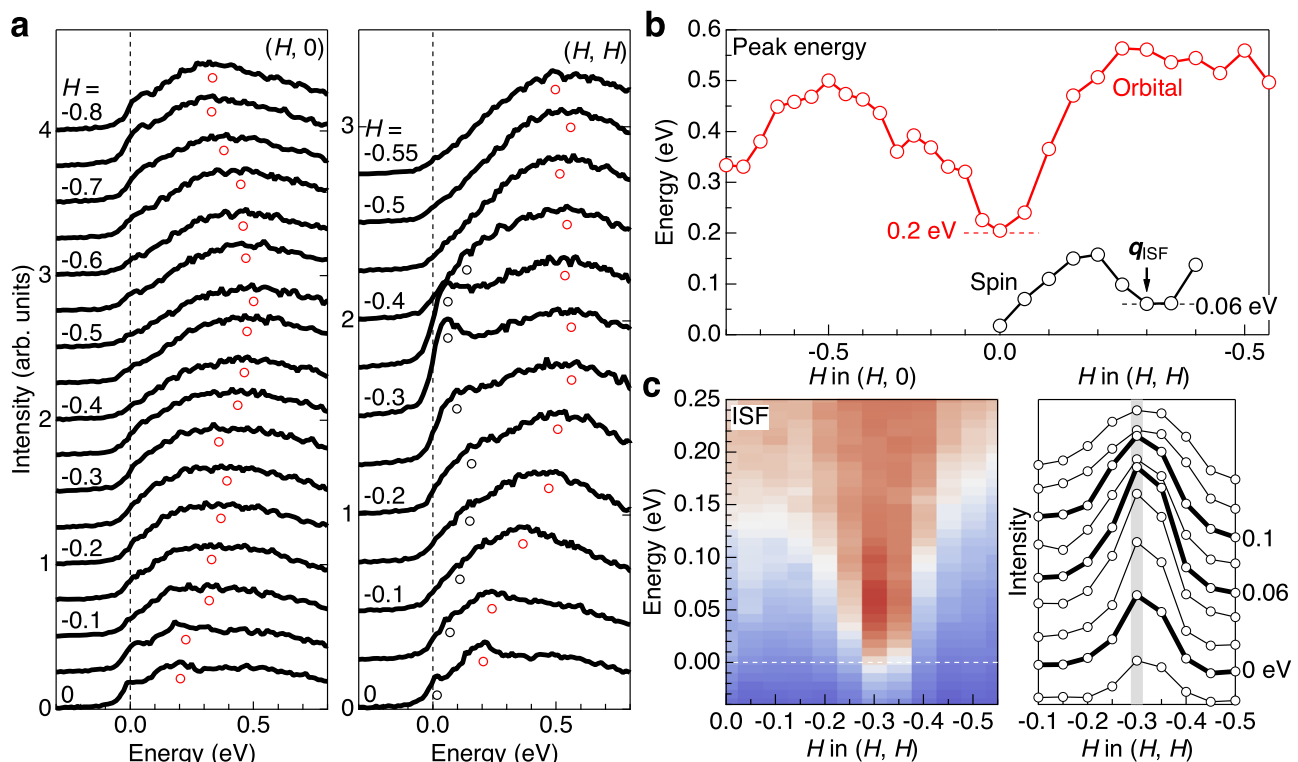


Fig. 2 | Spin and orbital fluctuations within the t_{2g} orbitals. **a** Expanded plots of low-energy RIXS spectra. The global peak maxima corresponding to the orbital fluctuations are indicated by red circles. Along the (H, H) direction, the local maxima and shoulder structures from spin fluctuations are indicated with black circles. **b** Dispersion relations of the spin and orbital fluctuations as a function of the in-plane momentum transfer. The dispersion of the spin fluctuations is defined

as the maxima of local spectral curvature deduced from the second derivative analysis, and that of orbital fluctuations as the global maxima of the original RIXS spectra. The typical error bars associated with the numerical maximum search are smaller than the marker size. **c** Expanded colormap of RIXS intensity around the ISF. The right panel shows momentum distribution curves with a step of 0.02 eV.

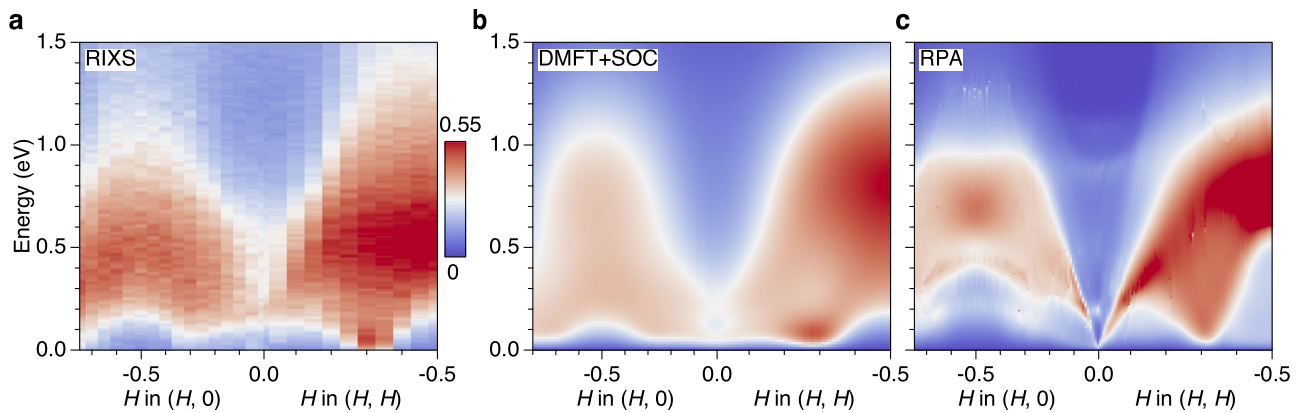


Fig. 3 | Modelling of RIXS spectra by DMFT+SOC calculations. **a** Expanded colormap of the RIXS intensity within the t_{2g}^4 electron configurations. **b** Simulation of RIXS intensity based on the spin and orbital susceptibilities calculated by the

dynamical mean-field theory with spin-orbit coupling (DMFT+SOC). **c** Simulation from the susceptibilities calculated with the random phase approximation (RPA).

The RIXS intensity around \mathbf{q}_{ISF} shows a conical shape with an isolated intensity maximum at 0.06 eV. The intensity remains centered at \mathbf{q}_{ISF} up to 0.25 eV, consistent with the vertical INS intensity profile at \mathbf{q}_{ISF} observed below -0.06 eV³⁰.

We now interpret the low-energy RIXS data in terms of theoretical spin and orbital susceptibilities $\chi_{S_{\mu}S_{\mu}}$ and $\chi_{L_{\mu}L_{\mu}}$ ($\mu = x, y, z$), which we computed in DMFT by solving the Bethe-Salpeter equation using the local DMFT particle-hole irreducible vertex within the Ru $4d-t_{2g}$ subspace (Supplementary Note 3). We employed the same effective model and interaction parameters that have been established in several previous studies^{31–33}. Theoretical RIXS spectra are constructed by combining different components of the spin and orbital susceptibilities with matrix elements for the RIXS cross section (Supplementary Note 4). Figure 3 shows the comparison of the experimental (Fig. 3a) and theoretical DMFT (Fig. 3b) RIXS spectra along the previously defined high-symmetry momentum paths in the Brillouin zone. To highlight the importance of the DMFT dynamical vertex corrections, we also show the perturbative RPA spectra (without dynamical vertex) in Fig. 3c. It is evident that the DMFT spectra excellently capture the overall dispersion and the distribution of momentum and energy dependent maxima of the RIXS data. Specifically, the low-energy intensity is peaked at \mathbf{q}_{ISF} and also extrapolates continuously to the corresponding quasistatic intensity close to zero energy³². Moreover, the broader maximum emanates from 0.2 eV at $\mathbf{q} = (0, 0)$ and disperses more steeply along the (H, H) direction. In contrast, the spectral weight distribution in RPA fails to capture the low-energy intensity maximum at \mathbf{q}_{ISF} and yields a spuriously sharp feature that extends from high energy to zero energy around the Γ point.

This difference between DMFT and RPA originates from the distinct behavior of the spin and orbital dynamical responses. Figure 4 shows the intensity plots of theoretical orbital (LL) and spin (SS) susceptibilities along the $\mathbf{q} = (H, 0)$ and (H, H) directions, obtained by averaging all components $\frac{1}{3}\sum_{\mu}\chi_{L_{\mu}L_{\mu}}$ and $\frac{1}{3}\sum_{\mu}\chi_{S_{\mu}S_{\mu}}$. The vertex corrections in DMFT lead to the clear energy separation of spin and orbital contributions predicted for the Hund metals (left panels). The spin response accounts for almost all the spectral weight at low energies up to -0.2 eV, and becomes negligible above this scale. The concentrated spectral weight around \mathbf{q}_{ISF} and weak ridge scattering around $\mathbf{q} = (-0.3, 0)$ and $(-0.7, 0)$ excellently reproduce the experimental observations. The orbital response sets in at higher energies > 0.2 eV and shows broad maxima centered around commensurate momenta $\mathbf{q} = (-0.5, 0)$ and $(-0.5, -0.5)$. In RPA (right panels), on the other hand, both the spin- and orbital responses disperse and have spectral weight over the entire energy range. The RIXS data thus provide direct and quantitative evidence for the spin-orbital separation in correlated Hund metals as captured by DMFT. Further improvement between the experiment and theory could

be obtained by a more rigorous treatment of the resonance effect in the RIXS cross section, in particular on the spectral weight maximum of the orbital excitations around $\mathbf{q} = (-0.5, -0.5)$.

It should also be noted that the spin-orbit coupling (SOC) effects have been considered only outside the vertex in our DMFT calculations. Comparison to angle-resolved photoemission experiments³¹ and inelastic neutron-scattering³² have justified this procedure on the level of the single-particle spectra and static magnetic susceptibility. The excellent agreement we find in the present work supports the strategy also for the dynamic susceptibility. This situation is contrasted to the spin-orbital J physics in the Mott insulating counterpart Ca_2RuO_4 ²⁷ and the cubic K_2RuCl_6 ³⁴, whose magnetic ground states are determined by the interplay between the ionic J multiplets and the strength of inter-site exchange interactions. While the t_{2g} electrons of Sr_2RuO_4 carry orbital angular momentum, the finite bandwidth of the itinerant electrons partially quenches the orbital momentum. Nonetheless, the SOC brings about significant modification of the single-particle band structure at certain high-symmetry momenta in the Brillouin zone, when multiple bands are degenerate in energy. It is well known that in Sr_2RuO_4 this degeneracy occurs in the diagonal direction in the reciprocal space, which leads to the separation of the Fermi-surface sheets^{31,35}. Correspondingly, the effect of SOC on the dynamical susceptibilities is most pronounced in the low-energy spin fluctuations at $\mathbf{q} = (0, 0)$ and at \mathbf{q}_{ISF} , while the effect on the orbital fluctuations remains minor (Supplementary Fig. 8).

The current findings also have implications for the microscopic mechanisms of the superconductivity in Sr_2RuO_4 . As primary candidates of bosonic fluctuations mediating the Cooper pairing, the spin and orbital dynamical susceptibilities enter the Eliashberg equations, which in turn determine the SC order parameter. Our combined RIXS and DMFT+SOC results provide a comprehensive description of the momentum distribution, dispersion relation, and spin-orbit composition of low-energy magnetic excitations, which can serve as crucial input for approximate solutions of the Eliashberg equations. Recent theoretical studies suggest that static (RPA) and dynamic (DMFT) vertex approximations lead to qualitatively different SC ground states^{33,36–38}. Although computational challenges prohibit rigorous extrapolation of our theoretical results to low temperatures near $T_c = 1.5$ K, the RIXS data point to the critical role of dynamical vertex corrections also for the microscopic description of the superconducting order parameter.

In conclusion, we have presented Ru L_3 RIXS measurements of the dynamical response functions in the unconventional superconductor Sr_2RuO_4 over a broad range of energy and momentum. We have identified several branches of spin and orbital excitations and revealed the separation of energy scales associated with these two sets of

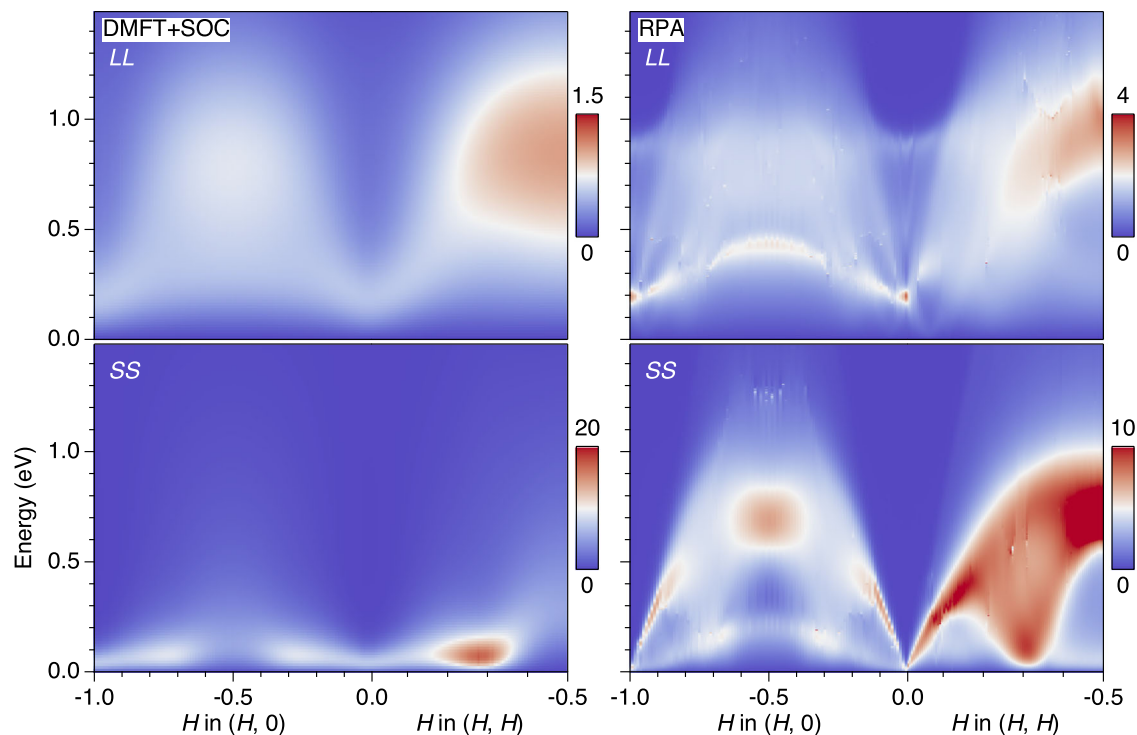


Fig. 4 | Spin-orbital energy scale separation in DMFT+SOC. Theoretical orbital (LL) and spin (SS) susceptibilities obtained by averaging all components, $\frac{1}{3}\sum_{\mu} \chi_{L_{\mu}L_{\mu}}$ and $\frac{1}{3}\sum_{\mu} \chi_{S_{\mu}S_{\mu}}$, calculated with DMFT+SOC (left) and RPA (right).

degrees of freedom, a predicted hallmark of Hund metals which had not yet received direct experimental confirmation. The measured spectra are in excellent agreement with theoretical calculations based on DMFT including vertex corrections, while significant discrepancies with the perturbative RPA approximation are found. Our results thus epitomize the power of state-of-the-art many-body theories to yield a detailed, quantitative understanding of complex electronic correlation functions in real materials. By establishing the properties of key collective modes, they also provide a solid baseline for the future identification of the nature and symmetry of SC order in this prominent model compound.

Methods

Sample growth and characterization

The Sr_2RuO_4 single crystals with superconducting $T_c \sim 1.5$ K were grown by the floating-zone method³⁹ and pre-aligned using an in-house Laue diffractometer. Sr_2RuO_4 has the tetragonal space group $I4/mmm$ with the lattice constants of $a = b = 3.903$ and $c = 12.901$ Å. The in-plane momentum transfers are expressed in the reciprocal lattice units (r.l.u.).

RIXS spectrometer

The RIXS experiments were performed using the intermediate-energy RIXS (IRIXS) spectrometer at the P01 beamline of PETRA III at DESY⁴⁰. The incident x-ray energy was tuned to the Ru L_3 absorption edge (2838 eV) and incoming photons were monochromatized using a high-resolution monochromator composed of four asymmetrically-cut Si(111) crystals. The polarization of the incident x-ray photons was in the horizontal scattering plane (π polarization). The polarizations of the scattered photons were not analyzed. The x-rays were focused to a beam spot of $20 \times 160 \mu\text{m}^2$ (H \times V). Scattered photons from the sample were collected at the scattering angle of 90° (horizontal scattering geometry) using a SiO_2 (102) ($\Delta E = 60$ meV) diced spherical analyzer with a 1 m arm, equipped with a rectangular $[100$ (H) \times 36 (V) mm^2] mask and a CCD camera, both placed in the Rowland geometry.

Collected raw CCD images were transformed into RIXS spectra by summing over the vertical axis of the detector and by binning with 12.5 meV steps along the horizontal axis. To account for the x-ray self-absorption effect, the RIXS intensity was normalized to the total fluorescent intensity collected with an energy-resolved photon detector placed at the scattering angle of 110° . The exact position of the zero energy loss line was determined by measuring non-resonant spectra from silver paint deposited next to the sample. The overall energy resolution of the IRIXS spectrometer at the Ru L_3 -edge, defined as the full width half maximum of the non-resonant spectrum from silver, was ~ 80 meV. All the measurements were performed at 25 K (normal state), well above the superconducting T_c .

Data availability

The raw RIXS data generated in this study are available at desycloud: <https://desycloud.desy.de/index.php/s/LPt7RJTHqGWLNBd>.

Code availability

The numerical codes used to generate the results in this work are available at desycloud: <https://desycloud.desy.de/index.php/s/LPt7RJTHqGWLNBd>.

References

- Keimer, B., Kivelson, S. A., Norman, M. R., Uchida, S. & Zaanen, J. From quantum matter to high-temperature superconductivity in copper oxides. *Nature* **518**, 179–186 (2015).
- Li, D. et al. Superconductivity in an infinite-layer nickelate. *Nature* **572**, 624–627 (2019).
- Imada, M., Fujimori, A. & Tokura, Y. Metal-insulator transitions. *Rev. Mod. Phys.* **70**, 1039–1263 (1998).
- Fernandes, R. M. et al. Iron pnictides and chalcogenides: a new paradigm for superconductivity. *Nature* **601**, 35–44 (2022).
- Georges, A., Medici, L. D. & Mravlje, J. Strong correlations from Hund's coupling. *Annu. Rev. Condens. Matter Phys.* **4**, 137–178 (2013).

6. Stadler, K. M., Yin, Z. P., von Delft, J., Kotliar, G. & Weichselbaum, A. Dynamical mean-field theory plus numerical renormalization-group study of spin-orbital separation in a three-band Hund metal. *Phys. Rev. Lett.* **115**, 136401 (2015).
7. Horvat, A., Žitko, R. & Mravlje, J. Low-energy physics of three-orbital impurity model with Kanamori interaction. *Phys. Rev. B* **94**, 165140 (2016).
8. Mackenzie, A. P. & Maeno, Y. The superconductivity of Sr₂RuO₄ and the physics of spin-triplet pairing. *Rev. Mod. Phys.* **75**, 657–712 (2003).
9. Hussey, N. E. et al. Normal-state magnetoresistance of Sr₂RuO₄. *Phys. Rev. B* **57**, 5505–5511 (1998).
10. Maeno, Y. et al. Superconductivity in a layered perovskite without copper. *Nature* **372**, 532–534 (1994).
11. Pustogow, A. et al. Constraints on the superconducting order parameter in Sr₂RuO₄ from oxygen-17 nuclear magnetic resonance. *Nature* **574**, 72–75 (2019).
12. Ishida, K., Manago, M., Kinjo, K. & Maeno, Y. Reduction of the ¹⁷O Knight shift in the superconducting state and the heat-up effect by NMR pulses on Sr₂RuO₄. *J. Phys. Soc. Jpn.* **89**, 034712 (2020).
13. Petsch, A. N. et al. Reduction of the spin susceptibility in the superconducting state of Sr₂RuO₄ observed by polarized neutron scattering. *Phys. Rev. Lett.* **125**, 217004 (2020).
14. Rice, T. M. & Sigrist, M. Sr₂RuO₄: an electronic analogue of ³He? *J. Phys. Condens. Matter* **7**, L643–L648 (1995).
15. Ishida, K. et al. Spin-triplet superconductivity in Sr₂RuO₄ identified by ¹⁷O Knight shift. *Nature* **396**, 658–660 (1998).
16. Kivelson, S. A., Yuan, A. C., Ramshaw, B. & Thomale, R. A proposal for reconciling diverse experiments on the superconducting state in Sr₂RuO₄. *npj Quantum Mater.* **5**, 43 (2020).
17. Klein, Y. et al. Thermoelectric power in ruthenates: dominant role of the spin degeneracy term. *MRS Online Proceedings Library* **988**, 9880706 (2006).
18. Mravlje, J. & Georges, A. Thermopower and entropy: Lessons from Sr₂RuO₄. *Phys. Rev. Lett.* **117**, 036401 (2016).
19. Mravlje, J. et al. Coherence-incoherence crossover and the mass-renormalization puzzles in Sr₂RuO₄. *Phys. Rev. Lett.* **106**, 096401 (2011).
20. Kugler, F. B. et al. Strongly correlated materials from a numerical renormalization group perspective: How the Fermi-liquid state of Sr₂RuO₄ emerges. *Phys. Rev. Lett.* **124**, 016401 (2020).
21. Sidis, Y. et al. Evidence for incommensurate spin fluctuations in Sr₂RuO₄. *Phys. Rev. Lett.* **83**, 3320–3323 (1999).
22. Steffens, P. et al. Spin fluctuations in Sr₂RuO₄ from polarized neutron scattering: Implications for superconductivity. *Phys. Rev. Lett.* **122**, 047004 (2019).
23. Iida, K. et al. Horizontal line nodes in Sr₂RuO₄ proved by spin resonance. *J. Phys. Soc. Jpn.* **89**, 053702 (2020).
24. Jenni, K. et al. Neutron scattering studies on spin fluctuations in Sr₂RuO₄. *Phys. Rev. B* **103**, 104511 (2021).
25. Damascelli, A. et al. Fermi surface, surface states, and surface reconstruction in Sr₂RuO₄. *Phys. Rev. Lett.* **85**, 5194–5197 (2000).
26. Mazin, I. I. & Singh, D. J. Competitions in layered ruthenates: Ferromagnetism versus antiferromagnetism and triplet versus singlet pairing. *Phys. Rev. Lett.* **82**, 4324–4327 (1999).
27. Gretarsson, H. et al. Observation of spin-orbit excitations and Hund's multiplets in Ca₂RuO₄. *Phys. Rev. B* **100**, 045123 (2019).
28. Bertinshaw, J. et al. Spin and charge excitations in the correlated multiband metal Ca₃Ru₂O₇. *Phys. Rev. B* **103**, 085108 (2021).
29. Fatuzzo, C. G. et al. Spin-orbit-induced orbital excitations in Sr₂RuO₄ and Ca₂RuO₄: A resonant inelastic x-ray scattering study. *Phys. Rev. B* **91**, 155104 (2015).
30. Iida, K. et al. Inelastic neutron scattering study of the magnetic fluctuations in Sr₂RuO₄. *Phys. Rev. B* **84**, 060402 (2011).
31. Tamai, A. et al. High-resolution photoemission on Sr₂RuO₄ reveals correlation-enhanced effective spin-orbit coupling and dominantly local self-energies. *Phys. Rev. X* **9**, 021048 (2019).
32. Strand, H. U. R., Zingl, M., Wentzell, N., Parcollet, O. & Georges, A. Magnetic response of Sr₂RuO₄: Quasi-local spin fluctuations due to Hund's coupling. *Phys. Rev. B* **100**, 125120 (2019).
33. Käser, S. et al. Interorbital singlet pairing in Sr₂RuO₄: A Hund's superconductor. *Phys. Rev. B* **105**, 155101 (2022).
34. Takahashi, H. et al. Nonmagnetic J = 0 state and spin-orbit excitations in K₂RuCl₆. *Phys. Rev. Lett.* **127**, 227201 (2021).
35. Haverkort, M. W., Elfimov, I. S., Tjeng, L. H., Sawatzky, G. A. & Damascelli, A. Strong spin-orbit coupling effects on the Fermi surface of Sr₂RuO₄ and Sr₂RhO₄. *Phys. Rev. Lett.* **101**, 026406 (2008).
36. Acharya, S. et al. Evening out the spin and charge parity to increase T_c in Sr₂RuO₄. *Commun. Phys.* **2**, 163 (2019).
37. Gingras, O., Nourafkan, R., Tremblay, A.-M. S. & Côté, M. Superconducting symmetries of Sr₂RuO₄ from first-principles electronic structure. *Phys. Rev. Lett.* **123**, 217005 (2019).
38. Gingras, O., Allaglo, N., Nourafkan, R., Côté, M. & Tremblay, A.-M. S. Superconductivity in correlated multiorbital systems with spin-orbit coupling: Coexistence of even- and odd-frequency pairing, and the case of Sr₂RuO₄. *Phys. Rev. B* **106**, 064513 (2022).
39. Bobowski, J. S. et al. Improved single-crystal growth of Sr₂RuO₄. *Condens. Matter* **4**, 6 (2019).
40. Gretarsson, H. et al. IRIXS: a resonant inelastic X-ray scattering instrument dedicated to X-rays in the intermediate energy range. *J. Synchrotron Rad.* **27**, 538–544 (2020).

Acknowledgements

We thank A. Damascelli, G. Khaliullin, A. Yaresko, and D. Kukusta for enlightening discussions. We acknowledge DESY (Hamburg, Germany), a member of the Helmholtz Association HGF, for the provision of experimental facilities. The RIXS experiments were carried out at the beamline P01 of PETRA III at DESY. The project was supported by the European Research Council under Advanced Grant No. 669550 (Com4Com) awarded to B.K.. H.S. acknowledges financial support from the JSPS Research Fellowship for Research Abroad and Grants-in-Aid for Scientific Research from JSPS (KAKENHI) (number 22K13994). H.S. and L.W. acknowledge financial support from the Alexander von Humboldt Foundation. S.K. acknowledges financial support by the DFG project HA7277/3-1. H.U.R.S. acknowledges financial support from the ERC synergy grant (854843-FASTCORR). N.K. is supported by KAKENHI (Grant Nos. 18K04715, 21H01033, and 22K19093), Core-to-Core Program (No. JPJSCCA20170002) from JSPS, and a JST-Mirai Program (Grant No. JPMJMI18A3). Research in Dresden benefits from the environment provided by the DFG Cluster of Excellence ct.qmat (EXC 2147, project ID 390858940) awarded to A.P.M.. The Flatiron Institute is a division of the Simons Foundation.

Author contributions

H.S., L.W., J.B., Z.Y., and H.G. performed the RIXS experiments. M.K., F.J., N.K., and A.P.M. grew the Sr₂RuO₄ single crystals. H.S., L.W., and M.K. performed the sample characterizations. H.G. designed the beamline and IRIXS spectrometer. H.S. analyzed the experimental data. H.U.R.S., S.K., N.W., and O.P. developed the computational framework used in the theoretical calculations. S.K., H.U.R.S., A.G., and P.H. carried out the theoretical calculations of the dynamical response functions. H.S. and P.H. constructed the theoretical RIXS intensity from the response functions. H.S., S.K., H.U.R.S., A.G., P.H., and B.K. wrote the manuscript with input from all the co-authors. B.K. initiated and supervised the project.

Funding

Open Access funding enabled and organized by Projekt DEAL.

Competing interests

The authors declare no competing interests.

Additional information

Supplementary information The online version contains supplementary material available at <https://doi.org/10.1038/s41467-023-42804-3>.

Correspondence and requests for materials should be addressed to H. Suzuki, H. Gretarsson or B. Keimer.

Peer review information *Nature Communications* thanks the anonymous, reviewer(s) for their contribution to the peer review of this work. A peer review file is available.

Reprints and permissions information is available at <http://www.nature.com/reprints>

Publisher's note Springer Nature remains neutral with regard to jurisdictional claims in published maps and institutional affiliations.

Open Access This article is licensed under a Creative Commons Attribution 4.0 International License, which permits use, sharing, adaptation, distribution and reproduction in any medium or format, as long as you give appropriate credit to the original author(s) and the source, provide a link to the Creative Commons licence, and indicate if changes were made. The images or other third party material in this article are included in the article's Creative Commons licence, unless indicated otherwise in a credit line to the material. If material is not included in the article's Creative Commons licence and your intended use is not permitted by statutory regulation or exceeds the permitted use, you will need to obtain permission directly from the copyright holder. To view a copy of this licence, visit <http://creativecommons.org/licenses/by/4.0/>.

© The Author(s) 2023